Journal of the Optical Society of America A
OPTICS, IMAGE SCIENCE, AND VISION

Characterization of the photoelastic dispersion coefficient using polarized digital holography

Sidney Leal da Silva,[1] Felipe Maia Prado,[2,*] Daniel José Toffoli,[1] and Niklaus Ursus Wetter[2]

[1]Optics and Applications Group, Fatec Itaquera, Zip code 08295-005, São Paulo, SP, Brazil
[2]Lasers and Applications Center, IPEN-CNEN/SP, Zip code 05508-000, São Paulo, Brazil
*felipemp369@gmail.com

Received 1 December 2022; revised 17 February 2023; accepted 20 February 2023; posted 22 February 2023; published 27 March 2023

The photoelastic dispersion coefficient represents the relationship between stress and the differences in refractive indices in a birefringent material. However, determining the coefficient using photoelasticity is challenging, as it is difficult to determine the refractive indices within photoelastic samples that are under tension. Here we present, for the first time, to our knowledge, the use of polarized digital holography to investigate the wavelength dependence of the dispersion coefficient in a photoelastic material. A digital method is proposed to analyze and correlate the differences in mean external stress with differences in mean phase. The results confirm the wavelength dependence of the dispersion coefficient, with an accuracy improvement of 25% compared to other photoelasticity methods.

https://doi.org/10.1364/JOSAA.482543

1. INTRODUCTION

The study of material properties can benefit from nondestructive techniques such as polarized digital holography (PDH) and the use of photoelastic materials [1–3]. Photoelastic materials exhibit temporary birefringence, and due to their transparency and elasticity they are utilized in various fields such as industry, for determining material properties, and dentistry for examining stress distributions caused by chewing [4–7]. PDH is a branch of holography that records and reconstructs light intensities and phases through interferometric techniques with polarizers and digital methods based on the Huygens–Fresnel diffraction theory [8–11].

Birefringence, also known as double refraction, was first described in the 17th century, by Erasmus Bartholinus, and later related to the stress and strain state of materials by David Brewster [12–16]. Photoelasticity saw significant progress in the 1950s and gained more sophistication with the advent of optical instruments combining polarizers and wave plates in the 1980s [17–20]. Many works with photoelasticity depend heavily on analytical equations to calculate the stress plane and the number of fringes of the sample under tension, which can result in a straightforward calculation, but only if all the required conditions and approximations are satisfied [6,7] Despite the advantages of photoelasticity, its optical measurements of refractive indices, phase differences, and other parameters are not obtained directly, resulting in a reliance on indirect and comparative statistical methods [3]. Holographic techniques, on the other hand, have made significant strides in recent years, yet not much research has been devoted to the quantitative analysis of stress and deformation using holography. Nevertheless, the dynamic nature of holography allows for more precise results, since it is founded on direct optical properties, including intensity, phase, refractive index, and others. This enables holography to hold significant potential for more thorough and quantitative analyses.

Holography is a branch of optics that involves the recording and reconstruction of light intensities and phases as they interact with materials [8–11]. The concept was first proposed by Hungarian physicist Gabor in 1948 and gained greater interest in the 1960s with the advent of the laser [21,22]. The coherent light produced by the laser, combined with the off-axis recording technique developed by Leith and Upatnieks in 1962, resulted in an increase in the quality of holographic images and motivated further research [23]. The significance of holography in the scientific world was acknowledged in 1971 when Dennis Gabor was awarded the Nobel Prize in Physics.

With the rise of computing power starting in the 1970s, holography evolved into digital form, enabling faster processing and greater accessibility [24,25]. Several methods now exist for reconstructing digital holograms, primarily based on convolution and Fresnel theories [3,26,27]. Digital holography (DH), utilizing non-destructive procedures, provides quantitative intensity and phase information of light transmitted through photoelastic materials. DH, when combined with appropriate statistical processing, produces highly accurate, quantitative results [28]. Holographic techniques utilizing polarizers for producing holograms of specific orientations and digital reconstruction methods for determining mechanical

material properties have been explored since 2000 and have shown promising outcomes in recent years [29,30].

The photoelastic dispersion coefficient (DC) is a crucial, wavelength-dependent parameter in photoelasticity studies that characterizes the material [31]. Its determination, which was first achieved through photoelasticity methods for photoelastic materials in works by Iyengar [32], Dixon [33], Souza *et al*. [34], Soares [35], Pawar [36], and Kuske [37], is crucial for understanding the relationship between elasticity and optics. The determination of DC through holography, however, has not been recorded. The significance of this lies in the ability to establish a direct relationship between the reconstructed phase from the hologram and the stress state of a photoelastic sample. This allows for the determination of stress differences through phase differences at each internal point of the sample, leading to the creation of a quantitative map of stress distribution due to externally applied efforts. For instance, in the field of dentistry where photoelastic materials are used to simulate masticatory efforts, this approach would be highly innovative and yield more quantifiable results.

The objective of this study is to assess the correlation between the photoelastic DC and the wavelength of light in a photoelastic material sample using a novel DH analysis approach that is capable of increasing the overall accuracy [3]. The data were obtained through a holographic method based on a modified Mach–Zehnder interferometer [38–40], where linear polarizers with orthogonally polarized states were incorporated before and after the sample in the object wave path. The reference wave path also incorporated a polarizer with the same polarization state as the last polarizer of the object wave. The experiment was conducted using two laser light sources, emitting at 632 and 543 nm. The validity of the technique was verified via calibration using a $\lambda/4$ wave plate that, depending upon a plate rotation angle, altered the polarization state of the object wave.

2. THEORY

A. Object and Reference Wave Functions

When the laser-emitted non-polarized wave ($\vec{\psi}$), with amplitude $\vec{A}$ and initial phase $e^{i\phi(0)}$, passes through a 50:50 beam splitter, it creates two separate waves, each with half the amplitude of the incident light, called object ($\vec{\psi}_{\mathrm{OBJ}}$) and reference ($\vec{\psi}_{\mathrm{REF}}$), represented in Eq. (1):

$$\vec{\psi}_{\mathrm{OBJ}}(\vec{r},t)=\vec{\psi}_{\mathrm{REF}}(\vec{r},t)=\frac{1}{2}\vec{A}e^{i\phi(0)}. \tag{1}$$

A linear polarizer, with a horizontal polarization state (90°), is placed in the path of the reference wave, as shown in Fig. 1. Equation (2) describes the resultant reference wave function, after the polarizer:

$$\vec{\psi}_{\mathrm{REF}}(\vec{r},t)=\frac{1}{2}e^{i\phi(0)}\begin{bmatrix}\vec{A}_{\hat{x}}\,e^{i\phi_{\mathrm{ref}(\hat{x})}}\\0\end{bmatrix}e^{i\phi(\vec{k},\vec{r})}$$

$$\equiv\vec{\psi}_{\mathrm{REF}}(0)\begin{bmatrix}e^{i\phi_{\mathrm{ref}(\perp)}}\\0\end{bmatrix}, \tag{2}$$

where $\vec{A}_x$ represents the wave amplitude in direction x, and $e^{i\phi(\vec{k},\vec{r})}$ represents the optical path difference between the object and reference waves.

Two linear polarizers, orthogonal to each other, are placed in the path of the object wave, as shown in Fig. 1. Between the polarizers, a $\lambda/4$ wave plate is placed for calibration of the configuration:

$$\vec{\psi}_{\mathrm{OBJ}(||)}(\vec{r},t)=\frac{1}{2}e^{i\phi(0)}\begin{bmatrix}0\\\vec{A}_{\hat{y}}\,e^{i\phi_{\mathrm{obj}(\hat{y})}}\end{bmatrix}e^{i\phi(\vec{k},\vec{r})}$$

$$\equiv\vec{\psi}_{\mathrm{OBJ}}(0)\begin{bmatrix}0\\e^{i\phi_{\mathrm{obj}(||)}}\end{bmatrix}. \tag{3}$$

The $\lambda/4$ wave plate, when rotated at an angle δ, produces a change in the polarization state, and the object wave becomes

$$\vec{\psi}_{\mathrm{OBJ}(\delta)}(\vec{r},t)=\vec{\psi}_{\mathrm{OBJ}}(0)\begin{bmatrix}e^{i\phi_{\mathrm{obj}(\perp)}}\\e^{i\phi_{\mathrm{obj}(||)}}\end{bmatrix}. \tag{4}$$

The second polarizer, in the path of the object wave, allows the passing of the wave only $\hat{x}$ in direction (orthogonal $\perp$):

$$\vec{\psi}_{\mathrm{OBJ}}(\vec{r},t)=\vec{\psi}_{\mathrm{OBJ}(\perp)}(\vec{r},t)=\vec{\psi}_{\mathrm{OBJ}}(0)\begin{bmatrix}e^{i\phi_{\mathrm{obj}(\perp)}}\\0\end{bmatrix}. \tag{5}$$

After the second 50:50 beam splitter, the final wave is the result of the interference between object and reference waves, both with a quarter amplitude of the original wave, as shown in Fig. 1 and Eq. (6):

$$\vec{\psi}(\vec{r},t)=\vec{\psi}'_{\mathrm{OBJ}}(\vec{r},t)+\vec{\psi}'_{\mathrm{REF}}(\vec{r},t)\Rightarrow\vec{\psi}(\vec{r},t)$$

$$=\vec{\psi}(0)\begin{bmatrix}e^{i\phi_{\mathrm{obj}(\perp)}}+e^{i\phi_{\mathrm{ref}(\perp)}}\\0\end{bmatrix}, \tag{6}$$

where $\vec{\psi}(0)=\overrightarrow{\psi}'_{\mathrm{OBJ}}(0)=\overrightarrow{\psi}'_{\mathrm{REF}}=(0)\,\frac{1}{4}e^{i\phi(0)}e^{i\phi(\vec{k},\vec{r})}$.

B. Calibration Equation

To perform the calibration of the holographic system it is necessary to find the phase difference of the resulting reconstructed wave, $\Delta\phi$, as a function of the rotation δ of the wave plate, such that

$$\Delta\phi=f(\delta). \tag{7}$$

Normalizing the object functions, we have

$$\vec{\psi}_{\mathrm{OBJ}}(\vec{r},t)=\vec{\psi}_{\mathrm{OBJ}}(0)\begin{bmatrix}0\\e^{i\phi_{\mathrm{obj}(||)}}\end{bmatrix}=\frac{1}{2}\begin{bmatrix}0\\1\end{bmatrix}, \tag{8}$$

where $\vec{\psi}_{\mathrm{OBJ}}(0)e^{i\phi_{\mathrm{obj}(||)}}=\frac{1}{2}$. Using the Jones rotation matrix [41],

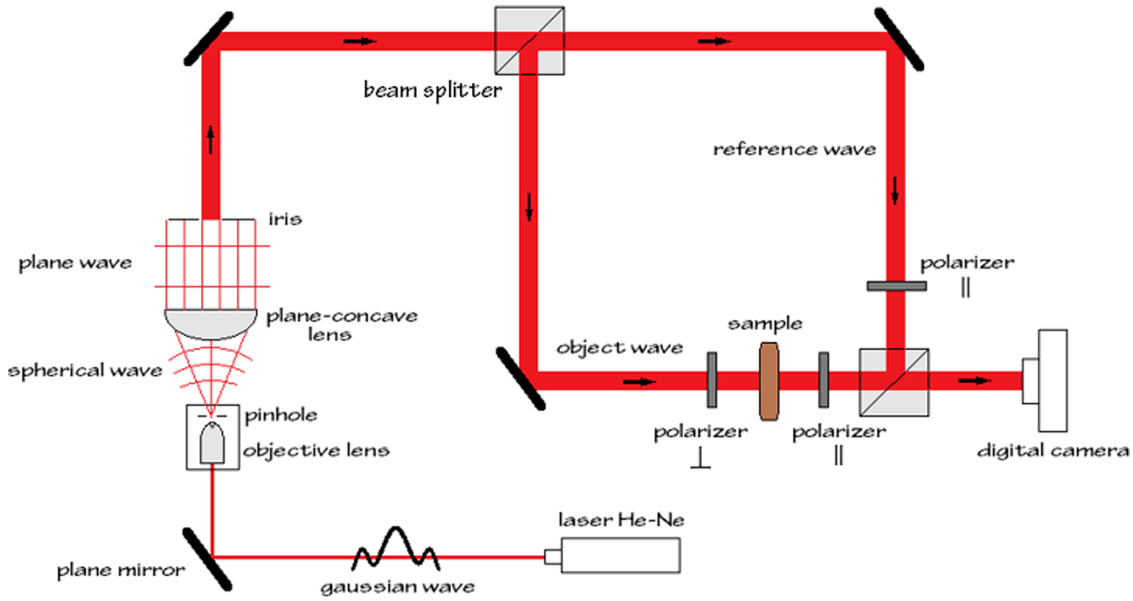

Fig. 1. Holographic setup composed of a Mach–Zehnder interferometer with orthogonal dichroic film polarizers.

$$\vec{\psi}_{\mathrm{OBJ}(\delta)}(\vec{r},t) = M(\delta)\vec{\psi}_{\mathrm{OBJ}}(\vec{r},t) = R(\delta)MR(-\delta)\frac{1}{2}\begin{bmatrix}0\\1\end{bmatrix}$$
$$\Rightarrow \vec{\psi}_{\mathrm{OBJ}(\delta)}(\vec{r},t) = \frac{1}{2}\begin{bmatrix}\mathrm{sen}(\delta)\cos(\delta)(i-1)\\ \cos^2(\delta) + i\,\mathrm{sen}^2(\delta)\end{bmatrix}$$
$$= \vec{\psi}_{\mathrm{OBJ}}(0)\begin{bmatrix}e^{i\phi_{\mathrm{obj}(\perp)}}\\ e^{i\phi_{\mathrm{obj}(\|)}}\end{bmatrix}$$
$$= \frac{1}{2}e^{i\phi_{\mathrm{obj}(\|)}}\begin{bmatrix}e^{i\Delta\phi_{\mathrm{obj}}}\\ 1\end{bmatrix}, \tag{9}$$

where $\vec{\psi}_{\mathrm{OBJ}}(0) = \frac{1}{2}e^{i\phi(0)}e^{i\phi(\vec{k},\vec{r})} = \frac{1}{2}$, and $\Delta\phi_{\mathrm{obj}} = \phi_{\mathrm{obj}(\perp)} - \phi_{\mathrm{obj}(\|)}$.

For $e^{i\phi_{\mathrm{obj}(\|)}} = 1$, the phase difference becomes

$$\Delta\phi_{\mathrm{obj}} = \mathrm{arctg}\left[-\cos(2\delta)\right]. \tag{10}$$

C. Photoelastic Dispersion Coefficient

Figure 2 presents the stress in the case of a parallelepiped of photoelastic material.

The optical information obtained from photoelasticity is related to the difference between the stresses in the directions along (σ_l) and perpendicular (σ_t) to the direction of the applied load, as given by the stress-optic law [34–37]

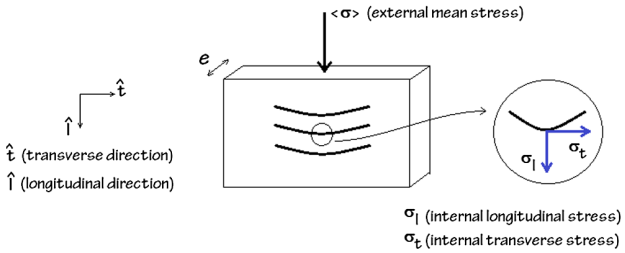

Fig. 2. Model of a photoelastic sample in the form a parallelepiped.

$$n_l - n_t = \frac{\lambda(1+\nu)}{eE}(\sigma_l - \sigma_t) = \frac{\lambda}{f_\sigma}(\sigma_l - \sigma_t) = \mathbb{C}(\sigma_l - \sigma_t), \tag{11}$$

where f_σ is the fringe number of the material, $\mathbb{C}(\lambda)$ is the optical dispersion, and $(n_l - n_t)$ is the difference between the indices of refraction in the directions longitudinal (n_l) and tranversal (n_t) to the effort. The phase difference is

$$\Delta\phi = \phi_l - \phi_t = \frac{2\pi}{\lambda}e(n_l - n_t), \tag{12}$$

where **e** is the sample thickness. Therefore, from Eqs. (11) and (12),

$$\sigma_l - \sigma_t = \frac{\lambda}{2\pi e\mathbb{C}}(\phi_l - \phi_t). \tag{13}$$

Similarly, in holography, a physical property of the material is defined as a reference point. This property is quantified as the fringe value obtained through holography [3] and can be defined as

$$\equiv \frac{e\mathfrak{E}}{a(1+\nu)}, \tag{14}$$

where ν is the Poisson's ratio, and a is a dimensionless constant that establishes the relationship between the holographic modulus of elasticity ($\mathfrak{E}$) and mechanical modulus of elasticity (E) of the material. Consequently, one can define the optical DC in holography in the same way as done in Eq. (11) for photoelasticity:

$$\mathcal{H} \equiv \frac{\lambda}{-} \equiv \frac{a(1+\nu)}{e\mathfrak{E}}\lambda. \tag{15}$$

Comparing the definition of $\mathbb{C}(\lambda)$, in Eq. (11) with the above defined $\mathcal{H}(\lambda)$, we conclude that

$$= f_\sigma \rightarrow \mathcal{H}(\lambda) = \mathbb{C}(\lambda). \tag{16}$$

Therefore, the stress-optic law for holography can be expressed as

$$\sigma_l - \sigma_t = \frac{\lambda}{2\pi e \mathcal{H}} (\phi_l - \phi_t) . \tag{17}$$

For consecutive external different efforts, one obtains

$$\sigma_{l(j)} - \sigma_{t(j)} = \frac{\lambda}{2\pi e \mathcal{H}} \left[\phi_{l(j)} - \phi_{t(j)}\right], \tag{18a}$$

$$\sigma_{l(j+1)} - \sigma_{t(j+1)} = \frac{\lambda}{2\pi e \mathcal{H}} \left[\phi_{l(j+1)} - \phi_{t(j+1)}\right]. \tag{18b}$$

Then, subtracting Eqs. (18b) and (18a),

$$\Delta\sigma_l - \Delta\sigma_t = \frac{\lambda}{2\pi e \mathcal{H}} (\Delta\phi_l - \Delta\phi_t) , \tag{19}$$

whereas $\Delta\sigma_l \sim \langle\sigma_{(j+1)}\rangle$ and $\Delta\phi_l \sim \langle\phi_{(j+1)}\rangle$ with parallel polarization, and $\Delta\sigma_t \sim \langle\sigma_{(j)}\rangle$ and $\Delta\phi_t \sim \langle\phi_{(j)}\rangle$ with perpendicular polarization. So, Eq. (19) can be rewritten as

$$\langle\Delta\sigma_{\text{external}}\rangle = \frac{\lambda}{2\pi e \mathcal{H}} \langle\Delta\phi\rangle, \tag{20}$$

where $\langle\Delta\sigma_{\text{external}}\rangle = \langle\sigma_{(j+1)}\rangle - \langle\sigma_{(j)}\rangle$, and $\langle\Delta\phi\rangle = \langle\phi_{(j+1)}\rangle - \langle\phi_{(j)}\rangle$.

As $\text{tg}(\gamma)$ is the slope of Eq. (20), $\mathcal{H}(\lambda)$ can be expressed as

$$\mathcal{H}(\lambda) = \frac{\lambda}{2\pi\ e\ \text{tg}(\gamma)}. \tag{21}$$

3. METHODOLOGY

A. Holographic Configuration

The holographic technique was based on a Mach–Zehnder interferometer [38–40] using, in part, a setup from previous experiments [42–45]. Figure 1 shows this scheme.

In the first part of the experiment, a red He–Ne laser was used, and in the second part, a green He–Ne laser. The laser emission was modified to a plane wave by a spatial filter using a 10× objective and a plane–concave lens. The interference pattern is formed at the second non-polarizing beam splitter where the two waves meet. This pattern was captured by a CMOS digital camera.

To calibrate the holographic setup, a $\lambda/4$ achromatic wave plate was used as a sample. The wave plate modified the polarization state of the wave at each angle, δ. For each angle of the wave plate, a hologram was registered that was stored for further analysis. The procedure was performed for both wavelengths. It is important to note that by using optical components suitable for the wavelengths of 632 and 543 nm, we ensure a better result and make it possible to reach a higher accuracy.

To determine the coefficient of photoelastic dispersion with the aid of the load device in Fig. 3(B), load sequences were performed on the photoelastic sample in Fig. 3(A). The procedure was repeated M times for each applied mass to allow the use of Gaussian distribution error propagation during the data analysis [46,47].

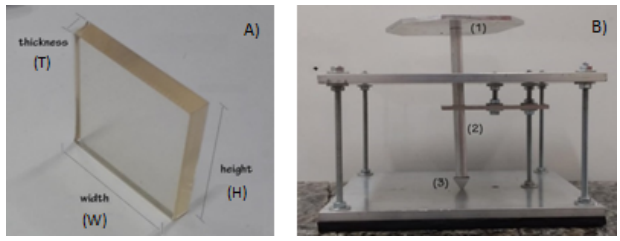

Fig. 3. (A) Photoelastic sample with general dimensions of thickness (T), width (W), and height (H). (B) Load device, to perform compressions of the sample, consisting of a plate for load placement (1), aluminum rod (2), and a triangular tip for the application of the stress.

B. Photoelastic Sample and Load Device

The sample used was a parallelepiped of epoxy resin-based photoelastic material in the solid phase. The main advantage of using this material associated with the polymerization process is the production of samples with excellent flexibilities and transparencies, ideal for the study of optics: photoelasticity, speckle and holography. The polymerization process allows samples to exhibit large amounts of photoelastic fringes when subjected to external stresses. All processes involving the sample preparation are described in detail in the paper of Da Silva [48]. Figure 3(A) presents the photo of the photoelastic sample utilized in our setup.

Using a digital caliper, 10 measurements in each of 10 different directions were made, in each dimension, width (W), height (H), and thickness (T), to justify the Gaussian statistical distribution process used to obtain the final results through error theory [46,47]. To perform the compressions on the sample, the load device of Fig. 3(B) was used.

The load device is basically composed of a (1) load base, (2) guiding rod, and (3) compression tip. The compressions were performed as follows.

Up to 10 loads of mass in grams were on the device. For each load, a short time interval Δt was given until the sample reached mechanical equilibrium.

For each load, a hologram of the interference pattern between object wave and reference wave was recorded. A hologram was also recorded with the unloaded sample to subtract the residual stresses contained in the sample.

C. Holographic Method

The photoelastic DCs were computed by programs that plotted the relationship between the mean efforts applied to the photoelastic sample and the average phase differences due to the induced stress. The phase images of the calibration and the photoelastic DCs were generated through a program based on the Fresnel method [3,27]. Custom algorithms were utilized to process a large volume of data, enhancing the accuracy of the results. The data were analyzed using Gaussian distributions and error theory principles [46,47].

During the determination of the photoelastic DC, the mean masses, the mean stress application areas in the samples that include the region of the application tip in contact with the upper surface of the sample, and their respective uncertainties

were found. Mean stress calculations were made using the mass means, local gravitational acceleration [49], and the mean application areas of the stresses on the sample. The uncertainties were determined by error propagations [46,47].

A hologram image and, after reconstruction, a phase map image were created for each load applied to the photoelastic sample. For each reconstructed image, an average of the pixel values of the phase map was taken. This average value was then used to calculate the phase difference between two different loads on the sample. Therefore, using Eq. (20), the relationship between the mean stresses and mean phases generated a set of experimental values, which was adjusted with the least squares method by a linear function. Finally, the photoelastic DCs were calculated by Eq. (21).

4. RESULTS

The He–Ne laser data were: 632.8 nm with 30 mW output power and 543.5 nm with 5 mW output power. The spatial filter was composed of an objective lens of 10× magnification and a pinhole with an aperture of 25 μm. The focal length of the concave lens was 20 cm. The digital resolution of the camera was 1280 × 1024 pixels (SXGA) with a total frame rate of 25 fps.

A. Calibration

In both setups, the wave plate was rotated from 0° to 360°, in steps of 5°. Figures 4(A) and 4(B) present the graph of the theoretical curve (–) and of the experimental values (+) of the relation between the phase difference (in degrees) and the rotation angle of the λ/4 wave plate for the red and green lasers, respectively.

From the experimental values of the graphs in Figs. 4(A) and 4(B), the following equations were obtained using the least-squares method [46,47]:

$$\Delta\phi_{\text{obj}}(\text{red}) = \text{arctg}[-\cos(2\delta + 3)] + 0.0125, \quad \textbf{(22a)}$$

$$\Delta\phi_{\text{obj}}(\text{green}) = \text{arctg}[-\cos(2\delta + 3)] + 0.0025. \quad \textbf{(22b)}$$

The calibration factors of Eqs. (22a) and (22b) were considered when calculating the phase differences of the photoelastic DCs, in both holographic setups. The calibration results showed good agreement between the experimental values and the adjusted theoretical curves, proving the reliability of the holographic system.

B. Photoelastic Dispersion Coefficient

The standard uncertainty of the caliper used to measure the geometric parameters of the photoelastic test sample was 0.01 mm. A set of 10 measurements was made for each of the 10 different directions randomly chosen for width, height, and thickness, resulting in (31.76 ± 0.09) mm width, (30.14 ± 0.07) mm height, and (4.85 ± 0.06) mm thickness.

Eleven different loads were placed over the photoelastic sample. The procedure was repeated 10 times. The local gravitational acceleration [49] in São Paulo, with a mean latitude of 23° and a mean altitude of 760 m sea level, is $g = (9.79 \pm 0.01)$ m/s^2. The mean area result was obtained from processing 100 values of length and width of the region of action of the compressor tip in the sample. These results were used in both experiments, with red and green lasers.

Figure 5 displays a photoelastic sample under tension in a linear polariscope and its respective hologram image. The isoclinic fringes produced by the use of a linear polarizer, despite causing problems in the photoelastic technique for the determinations of the DC, can be dealt with by simply choosing a region of the sample where the main contribution is the isochromatic fringes [50].

As is well known, the isoclinic fringes generate dark images that overshadow the isochromatic fringes, which are the sources of information for determining the relationships of internal deformation [50]. This is a main concern with photoelastic techniques, requiring the addition of λ/4 wave plates to diminish the isoclinic fringes. For holography, however, one can simply select the region of interest where the isoclinic fringes do not contribute strongly to the final hologram, as shown in Fig. 5.

Figures 6(A) and 6(B) present graphs of the mean stress versus relative mean phase for the experiment with the red and green lasers, respectively. The values (+) represent the experimental mean obtained, and the curve (−) represents the best fit, by error theory [46,47].

The curves in Fig. 6(A) and Fig. 6(B) present slopes of (0.604 ± 0.015) MPa and (0.705 ± 0.018) MPa for wavelengths of 632.8 and 543.5 nm, respectively. The

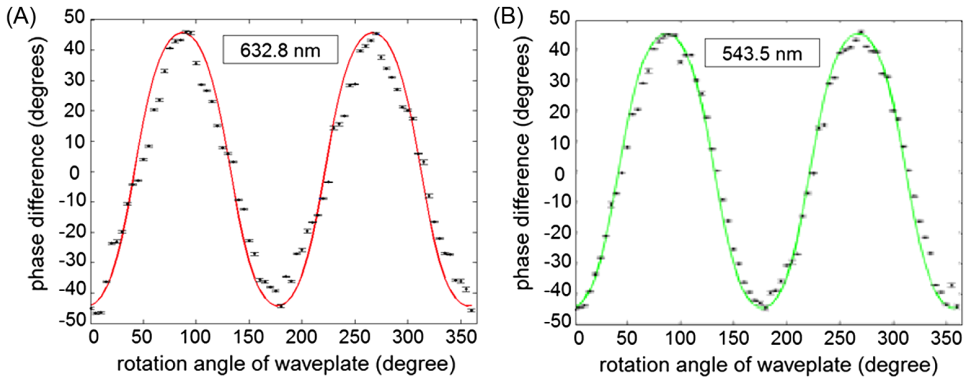

Fig. 4. (A) Theoretical graph (−) and experimental values (+) of the phase difference versus the rotation angle of the λ/4 wave plate (red laser). (B) Theoretical graph (−) and experimental values (+) of the phase difference versus the rotation angle of the λ/4 wave plate (green laser).

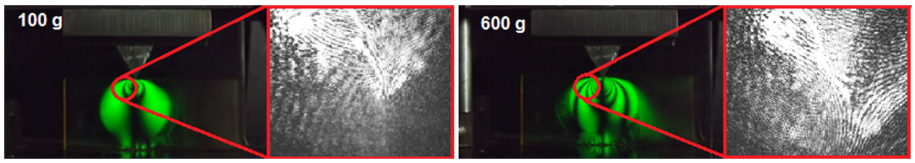

Fig. 5. Photoelastic sample under tension in a linear polariscope. The image couples on the right and left represent applied loads of 100 g and 600 g, respectively. Images with borders outlined in red represent the hologram of the selected region of the photoelastic sample.

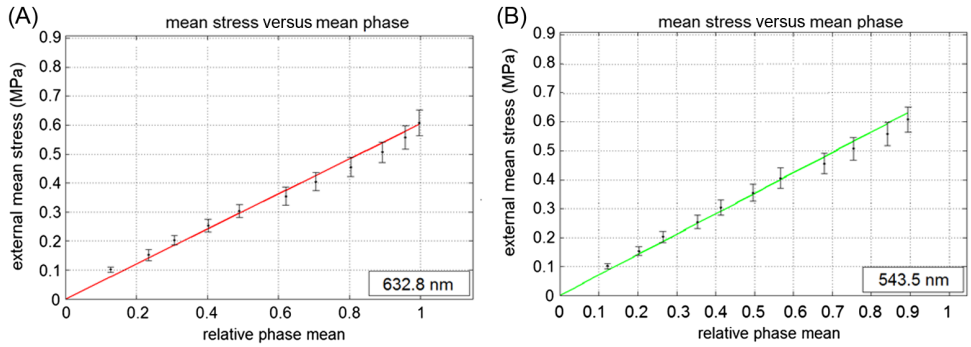

Fig. 6. (A) Adjusted best (−) and experimental values (+) mean stress versus relative mean phase for the experiment with the red laser. (B) Theoretical graph (−) and experimental values (+) mean stress versus relative mean phase for the experiment with the green laser.

wavelength-dependent photoelastic dispersion was calculated using Eq. (18).

The DCs obtained with the red and green lasers were $(3.44 \pm 0.10)\ 10^{-12}\ m^2/N$ and $(2.53 \pm 0.08)\ 10^{-12}\ m^2/N$, respectively. Additional measurements were made with a photoelastic sample with, approximately, half the width of the sample presented in Fig. 3(A), wielding a DC value of $(2.74 \pm 0.07)\ 10^{-12}\ m^2/N$ for the red laser.

In comparison, the values obtained with photoelasticity procedures presented in [3] for two samples of distinct concentrations, using red light, are $(5.32 \pm 0.22)\ 10^{-12}\ m^2/N$, and $(5.99 \pm 0.21)\ 10^{-12}\ m^2/N$. Despite the differences in the sample dimensions and in the concentration of the epoxy resin, the values of the DCs are comparable in terms of order of magnitude with the ones obtained indirectly by photoelasticity procedures.

The DCs ascertained through holography exhibited average uncertainties that were 44% lower than those reported in the literature. This finding points to enhanced accuracy, as seen by using the error theory treatment, primarily attributable to two factors: the substantial quantity of data obtained during the experiments, and the direct derivation of phase values from the reconstructed phase maps.

5. CONCLUSIONS AND PERSPECTIVES

By utilizing the photoelastic DC and the presented experimental setup, it is feasible to expeditiously and directly ascertain the internal stress values at every location of the photoelastic sample. The phase differences gathered from the reconstructed phase maps can then be compared to the theoretical values obtained via finite element simulation. As a result, the method and technique presented in this work provide an effective approach to determine the photoelastic DCs of photoelastic materials. It can be presented as an alternative in science and technology fields, offering the added benefits of expedience and ease for ascertaining the internal stress values at each point of the photoelastic sample.

An interesting application of this method is to investigate the effects of distinct materials inserted into photoelastic samples. For example, in the field of mechanical engineering, it is feasible to estimate the wear and fracture of composite materials, and in dentistry, it is possible to map and estimate the internal forces in the jaws, caused by prostheses.

An improvement to this work could be the implementation of reflection holography. This technique would enable the examination of stress versus strain distributions in various materials and potentially offer an alternative to the procedures used in industry today.

Funding. Fundação de Amparo à Pesquisa do Estado de São Paulo (2012/18162-4, 2019/23700-4).

Disclosures. The authors declare no conflicts of interest.

Data availability. Data underlying the results presented in this paper are not publicly available at this time but may be obtained from the authors upon reasonable request.

REFERENCES

1. F. Wang, Y. Zhang, H. Wang, W. Xu, Y. Zhang, and C. Li, "Nondestructive evaluation of residual stress via digital holographic photoelasticity," J. Opt. **47**, 547–552 (2018).
2. C. S. Narayanamurthy, G. Pedrini, and W. Osten, "Digital holographic photoelasticity," Appl. Opt. **56**, F213–F217 (2017).
3. S. L. da Silva, *Estudo de Tensões Em Amostras Fotoelásticas Com Holografia Digital* (Novas Edições Acadêmicas, 2017).
4. N. Parthasarathi, S. Srinivasa Senthil, M. Prakash, and K. S. Satyanarayanan, "Analytical and experimental study on reinforced concrete arch by photoelasticity technique," Asian J. Civ. Eng. **19**, 647–650 (2018).
5. H. A. Fandiño Toro, J. C. Briñez de León, A. Restrepo Martínez, and J. W. Branch Bedoya, "Análisis de campos de esfuerzos utilizando

fotoelasticidad visible e infrarroja," Visión electrónica **11**, 89–98 (2017).
6. J.-I. Lee, Y. Lee, Y.-L. Kim, and H.-W. Cho, "Effect of implant number and distribution on load transfer in implant-supported partial fixed dental prostheses for the anterior maxilla: a photoelastic stress analysis study," J. Prosthet. Dent. **115**, 161–169 (2016).
7. G. V. Portes, E. M. Boeck, N. Lunardi, and K. E. D. C. Pizzol, "Análise fotoelástica da distribuição da tensão após inserção de diferentes mini-implantes ortodônticos: estudo in vitro," Rev. Bras. Multidiscip. **20**, 71 (2017).
8. B. E. A. Saleh and M. C. Teich, *Fundamentals of Photonics*, Wiley Series in Pure and Applied Optics (Wiley, 1991).
9. M. Ferreira, *Óptica e Fotónica*, 1st ed. (Lidel-Edições Técnicas, 2003).
10. B. D. Guenther, *Modern Optics* (Oxford University, 2015).
11. E. Hecht, *Optics* (Pearson Education, 2012).
12. B. A. Moura, "Isaac Newton e a dupla refração da luz," Rev. Bras. Ensino Física **36**, 1–15 (2014).
13. B. W. François Bréhat, *Représentation Des États de Polarisation Des Ondes Lumineuses* (Editions Publibook, 2003).
14. J. A. Lohne, "Nova Experimenta Crystalli Islandici Disdiaclastici," Centaurus **21**, 106–148 (1977).
15. W. F. Magie, *Source Book in Physics* (Harvard University, 1969).
16. D. Brewster, "On the laws which regulate the polarization of light by reflection from transparent bodies," Proc. R. Soc. London **2**, 14–15 (1815).
17. M. M. Frocht, *A Special Investigation to Develop a General Method for Three-Dimensional Photoelastic Stress Analysis* (National Advisory Committee for Aeronautics, 1952).
18. E. G. Coker and G. L. N. Filon, *A Treatise on Photo-Elasticity* (University, 1931).
19. L. Föppl and E. Mönch, *Praktische Spannungsoptik* (Springer Berlin Heidelberg, 1950).
20. K. Ramesh, T. Kasimayan, and B. Neethi Simon, "Digital photoelasticity—a comprehensive review," J. Strain Anal. Eng. Des. **46**, 245–266 (2011).
21. D. Gabor, "A new microscopic principle," Nature **161**, 777–778 (1948).
22. M. Young, *Óptica e Lasers* (Edusp, 1998).
23. E. N. Leith and J. Upatnieks, "Reconstructed wavefronts and communication theory," J. Opt. Soc. Am. **52**, 1123 (1962).
24. M. A. Kronrod, N. S. Merzlyakov, and L. P. Yaroslavskii, "Computer synthesis of transparency holograms," JETP Sov. **17**, 329–332 (1972).
25. M. A. Kronrod, N. S. Merzlyakov, and L. P. Yaroslavskii, "Reconstruction of a hologram with a computer," JETP Sov. **17**, 333–334 (1972).
26. M. S. Z. Taietti, "Métodos recursivos para o cálculo da integral de convolução," Masters dissertation (Universidade Federal do Rio Grande do Sul, 2002).
27. V. C. Barbosa, A. M. S. Breitschaft, J. P. R. F. de Mendonça, L. M. Moreira, and P. C. G. de Moraes, "Uma visualização do princípio de Huygens-Fresnel na obtenção de um padrão de difração," Rev. Bras. Ensino Fís. **34**, 3301 (2012).
28. G. N. Oliveira, D. M. C. Rodrigues, L. C. S. Nunes, and P. A. M. dos Santos, "Digital Fourier transform holography applied to investigate mechanical deformation in polymers," Opt. Lasers Eng. **50**, 1798–1803 (2012).
29. T. Colomb, P. Dahlgren, D. Beghuin, E. Cuche, P. Marquet, and C. Depeursinge, "Polarization imaging by use of digital holography," Appl. Opt. **41**, 27–37 (2002).
30. M. Yokota, "Polarization analysis with digital holography by use of polarization modulation for single reference beam," Opt. Eng. **46**, 055801 (2007).
31. A. Kuske and G. Robertson, *Photoelastic Stress Analysis* (Wiley, 1974).
32. K. S. Iyengar, "Photo-elastic dispersion in cubic crystals," Nature **176**, 1119–1120 (1955).
33. R. W. Dixon and M. G. Cohen, "A new technique for measuring magnitudes of photoelastic tensors and its application to lithium niobate," Appl. Phys. Lett. **8**, 205–207 (1966).
34. F. L. Souza, G. A. Souza, and C. A. Araújo, "Determinação automática de parâmetros fotoelásticos," in *15o Simpósio Do Programa de Pós-Graduação Em Engenharia Mecânica* (2005).
35. W. A. Soares, "Determinação de parâmetros da mecânica de fratura a partir de imagens fotoelásticas, usando processamento digital," Instituto de Pesquisas Energéticas e Nucleares (1997).
36. S. S. Pawar, N. V. Patil, and H. V. Shete, "A review paper on stress analysis of leaf spring by using photo elaticity technique," Int. Res. J. Eng. Technol. **4**, 1475–1478 (2017).
37. A. Kuske and G. S. Robertson, *Photoelastic Stress Analysis* (Wiley-Interscience, 1974).
38. Q. Wang, G. Zhu, H. Chen, J. Jaques, J. Leuthold, A. B. Piccirilli, and N. K. Dutta, "Study of all-optical XOR using Mach-Zehnder interferometer and differential scheme," IEEE J. Quantum Electron. **40**, 703–710 (2004).
39. K. P. Zetie, S. F. Adams, and R. M. Tocknell, "How does a Mach-Zehnder interferometer work?" Phys. Educ. **35**, 46–48 (2000).
40. T. F. Ricci, F. Ostermann, and S. D. Prado, "O tratamento clássico do interferômetro de Mach-Zehnder: uma releitura mais moderna do experimento da fenda dupla na introdução da física quântica," Rev. Bras. Ensino Fís. **29**, 79–88 (2007).
41. T. Colomb, E. Cuche, F. Montfort, P. Marquet, and C. Depeursinge, "Jones vector imaging by use of digital holography: simulation and experimentation," Opt. Commun. **231**, 137–147 (2004).
42. D. M. Silva, E. A. Barbosa, and N. U. Wetter, "Simple and versatile heterodyne whole-field interferometer for phase optics characterization," Rev. Sci. Instrum. **83**, 103103 (2012).
43. D. M. da Silva, E. A. Barbosa, G. C. Cardoso, and N. U. Wetter, "Real-time contour fringes obtained with a variable synthetic wavelength from a single diode laser," Appl. Phys. B **118**, 159–166 (2015).
44. F. M. Prado, K. A. U. Utiyama, D. J. Toffoli, N. U. Wetter, and S. L. da Silva, "Computational algorithm from the Huygens-Fresnel's diffraction integral for two-dimensional holographic reconstruction," Rev. Bras. Ensino Fis. **44**, e20210193 (2021).
45. S. L. da Silva, F. M. Prado, D. J. Toffoli, and N. U. Wetter, "Measuring photoelastic dispersion coefficients in material samples with digital holography," Proc. SPIE **11306**, 148–154 (2020).
46. J. H. Vuolo, *Fundamentos Da Teoria de Erros* (Blucher, 2003).
47. F. J. MacWilliams and N. J. A. Sloane, *The Theory of Error-Correcting Codes* (Elsevier, 1999).
48. S. L. Silva, A. V. Lima, L. N. Da Silva, C. R. Da Silva, C. Gomes, E. G. R. Santos, H. S. Batista, and L. A. Ta Gein, "Análise qualitativa de tensões em estruturas sólidas acopladas a amostras de resina fotoelástica," Rev. Bras. Fís. Tecnol. Apl. **2**, 1–13 (2015).
49. W. Lopes, "Variação da aceleração da gravidade com a latitude e altitude," Cad. Bras. Ensino Fís. **25**, 561–568 (2008).
50. F. M. Prado, D. J. Toffoli, and S. L. da Silva, "Use of an automatic device for the determination of mechanical properties on photoelastic samples of small dimensions," Rev. Bras. Ensino Fis. **42**, e20200090 (2020).